Editors' Suggestion

Spin caloritronics in a $CrBr_3$-based magnetic van der Waals heterostructure

Tian Liu,[*,†] Julian Peiro,[†] Dennis K. de Wal, Johannes C. Leutenantsmeyer, Marcos H. D. Guimarães, and Bart J. van Wees
Zernike Institute for Advanced Materials, Nijenborgh 4, 9747 AG Groningen, The Netherlands

(Received 3 March 2020; revised manuscript received 11 April 2020; accepted 14 April 2020; published 6 May 2020)

The recently reported magnetic ordering in insulating two-dimensional (2D) materials, such as chromium triiodide (CrI_3) and chromium tribromide ($CrBr_3$), opens new possibilities for the fabrication of magnetoelectronic devices based on 2D systems. Inevitably, the magnetization and spin dynamics in 2D magnets are strongly linked to Joule heating. Therefore, understanding the coupling between spin, charge, and heat, i.e., spin caloritronic effects, is crucial. However, spin caloritronics in 2D ferromagnets remains mostly unexplored, due to their instability in air. Here we develop a fabrication method that integrates spin-active contacts with 2D magnets through hBN encapsulation, allowing us to explore the spin caloritronic effects in these materials. The angular dependence of the thermal spin signal of the $CrBr_3$/Pt system is studied, for different conditions of magnetic field and heating current. We highlight the presence of a significant magnetic proximity effect from $CrBr_3$ on Pt revealed by an anomalous Nernst effect in Pt, and suggest the contribution of the spin Seebeck effect from $CrBr_3$. These results pave the way for future magnonic devices using air-sensitive 2D magnetic insulators.

DOI: 10.1103/PhysRevB.101.205407

I. INTRODUCTION

The search for magnetism in 2D systems has been a nontrivial topic for decades. Recently, 2D magnetism was demonstrated in an insulating material CrI_3 [1], which shows antiferromagnetic exchange between the layers, resulting in zero (nonzero) net magnetization for even (odd) number of layers. It has been shown that $CrBr_3$ exhibits ferromagnetism when exfoliated down to a few layers [2] and monolayers [3] while preserving its magnetic order.

This discovery offers us a platform to explore magnonics in 2D systems. Magnonics refers to spintronics based on magnons, which are quantized spin waves, i.e., collective excitations of ordered electron spins in magnetic materials [4–6]. Magnonic spin transport has been extensively studied in various ways in 3D magnetic insulators, e.g., spin pumping [7], Spin Seebeck effect (SSE) [8], and electrical injection and detection of magnons [9]. The outstanding magnon transport properties of the ferrimagnetic insulator yttrium iron garnet (YIG) and the robustness and fast dynamic of AFM materials like iron oxide [10] and nickel oxide [11] triggered the development of the first magnon transport device prototypes for application using these materials [9,12,13]. The predicted novel physical phenomena [14–18] hosted by low-dimensional magnon systems represent a strong potential for 2D magnonics. Thermally excited magnon transport was reported recently in an AFM vdW 2D material $MnPS_3$ [19]. However, magnonics in 2D van der Waals magnetic systems still remains mostly unexplored, especially for 2D ferromagnetic (FM) systems.

One of the difficulties to study such phenomena is the easy degradation in air of the magnetic 2D materials, bringing extra technical challenges for integrating magnonic circuits with these materials. Here, we introduce a technique of bottom metallic contacts on an air-sensitive material $CrBr_3$, aiming at preliminary study of magnonics in 2D ferromagnetic materials. We select $CrBr_3$ as a medium for 2D magnonics study [20] as its FM order is independent on the number of layers and thus it simplifies the device fabrication. The Curie temperature of $CrBr_3$ is about $T_c = 37$ K [20] in bulk, reducing to 27 K for monolayers [3]. $CrBr_3$ presents perpendicular magnetic anisotropy (PMA) [2] with an out-of-plane coercive field of 4 mT and an in-plane saturation field of 400 mT for a few layers [3]. The saturation magnetization of about 271 kA/m is reported nearly equal for in-plane and out-of-plane orientation in bulk and differs by less than 20% for three-layer $CrBr_3$ [2,21].

II. DEVICE GEOMETRY AND MEASUREMENTS

In this work we employ nonlocal angular-dependent magnetoresistance (nlADMR) measurements on a hBN-encapsulated $CrBr_3$ flake contacted by Pt strips. ADMR measurements have been widely used to characterize the spin Hall magnetoresistance (SMR) in local geometries [22] or the spin Seebeck effect (SSE) in nonlocal geometry [9] and identify them out of other caloritronics effects [23–26]. We fabricated a device where Pt strips (5.5 nm thick) are deposited into a preetched 16.6-nm-thick hBN flake on top of a silicon oxide substrate. A 6.5-nm-thick top hBN flake is used to pick up and fully cover a 7-nm-thick $CrBr_3$ flake (about 10 layers) [27]. A schematic of the device and nonlocal measurement geometry is shown in Fig. 1(a).

[*]tian.liu@rug.nl
[†]These authors contributed equally to this work.

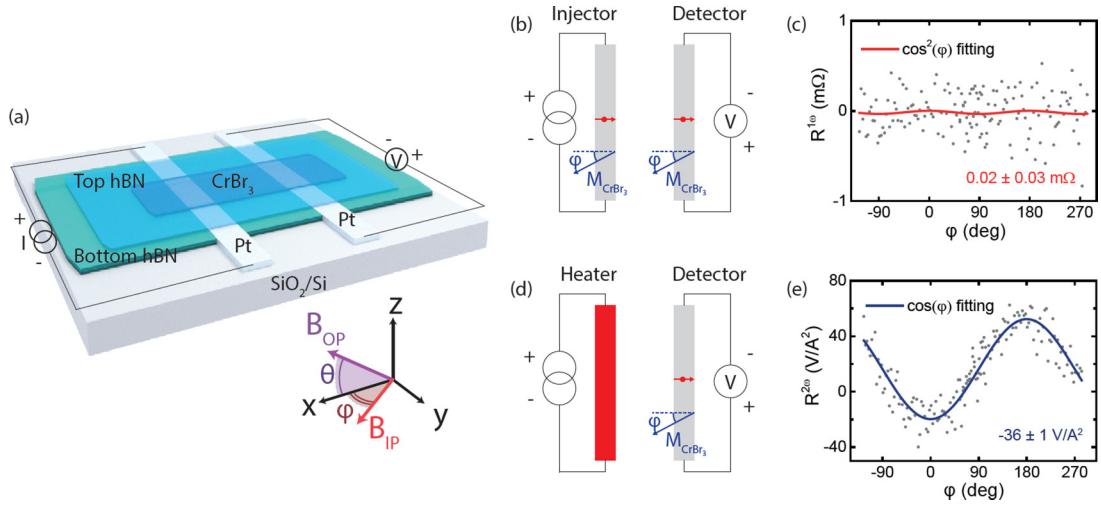

FIG. 1. (a) Schematic of the device and the circuit for the nonlocal measurements. A 7-nm-thick $CrBr_3$ flake placed on top of 5.5-nm-high Pt strips is fully encapsulated by two layers hBN. The x, y directions are defined to be in-plane (Pt strips parallel to the y axis), where the magnetic field is rotated over the azimuthal angle φ (IP) and polar angle theta (OOP). (b), (d) Principle of generation and detection of respectively electrically and thermally generated magnons. (c), (e) Measured corresponding first (c) and second (e) order harmonic NL resistances with 20 μA are fitted with the $\cos^2(\varphi)$ and $\cos(\varphi)$ function, respectively. The small red arrows in (b) and (d) indicate spin polarization direction. For (e) the sign of the fitted cosine for the ISHE from the SSE agrees with this spin polarization and therefore with the standard definition of the spin Hall angle [28]. For the measurement in (e), the offset $R_0^{2\omega} = 16.3 \pm 0.8$ V/A^2. The error bars represent the standard deviation from the fits.

In this system, a gradient of temperature is created by the Joule heating from a remote Pt heater which generates a magnon-mediated spin flow due to the magnon density dependence on the temperature [29], i.e., the SSE. At the interface between a magnet and a nonmagnetic material, a transfer of magnon spin ($+\hbar$) from the $CrBr_3$ to the Pt is possible by spin flip of a $-\hbar/2$ spin to a $+\hbar/2$ spin in the Pt. The spin current generated this way in the Pt contact converts into a charge current by inverse spin Hall effect (ISHE) and can be measured as a voltage difference. In the geometry defined in Fig. 1, the ADMR is then sensitive to the x component of the magnetization of $CrBr_3$, $\mathbf{M}_x$. In the in-plane ADMR configuration [Figs. 1(a) and 1(d)], the orientation of the magnetization with regard to the detection contact drives the angular dependence; therefore, a $\cos(\varphi)$ dependence is expected.

All data shown in the main text was measured on a pair formed of a 310-nm-wide injector and a 520-nm-wide detector, spaced by 500 nm edge to edge, and at a base temperature of 5 K under a reference magnetic field of 4 T, unless specifically mentioned. We separate different harmonics by using standard low frequency (6 Hz to 13 Hz) lock-in techniques. The voltage response is composed of different orders that are expanded as $V(t) = R_1 I(t) + R_2 I(t)^2 + \cdots$ [9], where R_i is the ith-order response [30] to the applied ac current $I(t)$. As the electrical magnon injection scales linearly with current, its response is expected in the first harmonic signal. The thermal injection depends quadratically on the applied current and the response appears in the second harmonic signal.

First and second harmonic responses of the nonlocal signal have been measured simultaneously all along this study. The first order angular dependence is expected to obey the relation $R^{1\omega} = V/I = R_0^{1\omega} + R_{\rm nl}^{1\omega}\cos^2(\varphi)$ [9], where $R_0^{1\omega}$ is an offset resistance and $R_{\rm nl}^{1\omega}$ is the magnitude of the first harmonic signal. However, we do not observe the expected $\cos^2(\varphi)$ modulation in the first harmonic signal, as the fitted first order resistance $R_{\rm nl}^{1\omega}$ is only detected in the order of 0.01 mΩ which is comparable to the standard deviation. An example of measured first harmonic signal can be found in Fig. 1(c). Yet, this value is at least three orders smaller than the $R_{\rm nl}^{1\omega}$ reported for the Pt/YIG system [9]). The measurements are carried out over a wide range of applied currents and magnetic fields, and with the maximum lock-in detection sensitivity. A typical measurement of first harmonic nonlocal signal is shown in Fig. 1(c), for a current of 20 μA at 5 K. In contrast, the nonlocal second harmonic signals exhibit a clear sinusoidal behavior [Fig. 1(e)] under an in-plane rotating magnetic field. The magnitudes of nonlocal signals were fitted with

$$R^{2\omega} = \frac{V}{I^2} = R_0^{2\omega} + R_{\rm nl}^{2\omega}\cos(\varphi), \tag{1}$$

where $R_0^{2\omega}$ is the offset resistance for the second harmonic signal. A nonzero offset $R_0^{2\omega}$ is always present, possibly from unintended Seebeck contribution in the detector [31]. $R_{\rm nl}^{2\omega}$ is the magnitude of the second harmonic signal. For the corresponding second harmonic measured in Fig. 1(e), we extract an amplitude $R_{\rm nl}^{2\omega} = -36 \pm 1$ V/A^2, which is comparable to the magnitude of room-temperature nonlocal SSE measured on bulk Pt/YIG samples [9] with equal angular dependence. If we compare to the typical top contact geometry used to detect SSE from YIG [9], the same SSE detected here in bottom contact geometry should produce a spin current in the opposite direction. Therefore, the ISHE induced in Pt is reversed compared to the top Pt on YIG; hence we expect an opposite sign of the signal. The negative sign observed here would correspond to the positive sign measured in [9] and, if attributed to SSE, reveals a transfer of magnon spin from $CrBr_3$ to the Pt top surface. However, at this point, we cannot

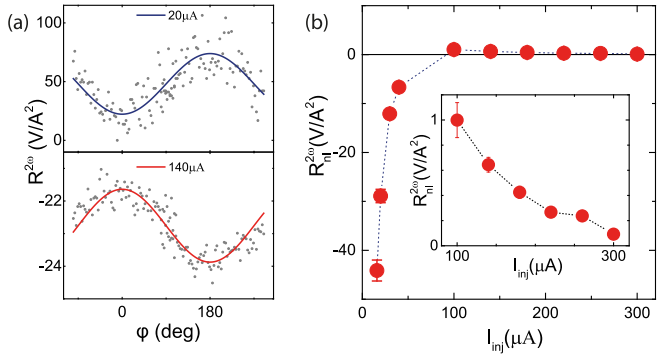

FIG. 2. Dependence of second harmonic signals on applied current through the injector. (a) Top panel: low bias signals with $\cos(\varphi)$ fitting measured at 20 μA, with a fitted amplitude $(-29 \pm 1\ \mathrm{V/A^2})$; bottom panel: high bias signals with $\cos(\varphi)$ fitting measured at 140 μA, with a fitted amplitude $(0.64 \pm 0.03\ \mathrm{V/A^2})$. (b) Bias dependence of $R^{2\omega}_{nl}$. Bias dependence shown in these graphs were measured at 5 K under a magnetic field of 4 T. The inner figure presents the zoom-in data of $R^{2\omega}_{nl}$, for the applied current from 100 μA to 300 μA.

rule out other effects like proximity induced anomalous Nernst effect (pANE) in Pt [32]. We discuss relevant effects later [see Fig. 4(c), rotation of out-of-plane magnetic field].

The current dependence of $R^{2\omega}_{nl}$ is plotted in Fig. 2, for a contact pair with distance of 950 nm center to center (edge to edge distance of 500 nm). $R^{2\omega}_{nl}$ depends on the applied current nonlinearly, and a sign reversal of $R^{2\omega}_{nl}$ occurs between 40 and 100 μA. For data measured at 60 μA and 80 μA, an angular modulation of the second harmonic signal is still observed but it is not described by a simple cosine function (see Supplemental Material [33]). An example of the negative $R^{2\omega}_{nl}$ at low current is shown in Fig. 2(a) (top panel), and an example of the positive $R^{2\omega}_{nl}$ at high current is plotted in Fig. 2(a) (bottom panel). The absolute amplitude $|R^{2\omega}_{nl}|$ in general decreases with increasing current at the heater, as plotted in Fig. 2(b). Its value for positive amplitude at high current is one to two orders of magnitude lower than its value for negative amplitude at low current, depending on the applied current.

To get better insight of the role of the complex temperature distribution in our device for this nonlinear behavior, we employ a two-dimensional finite element model (FEM) simulating a geometry of the x-z plane. Indeed the full hBN encapsulation of the $CrBr_3$ flake in this device brings inevitable additional heat conduction paths resulting in strong current-dependent thermal gradients in both x and z directions ($\partial_x T$ and $\partial_z T$, respectively). As κ_{CrBr_3}, the thermal conductivity of $CrBr_3$, is unknown, we ran the computation for different thermal conductance ratios η_K so that $\kappa_{CrBr_3}(T) = \eta_K\, \kappa_{hBN}(T)$, with κ_{hBN} the thermal conduction of hBN, and taking into account the highly temperature dependent thermal conduction of the materials (see Supplemental Material VII [33]). This modeling reveals a strong dependence of the temperature profile as a function of the heating current. It qualitatively supports that the main contribution of the thermal gradient in the Pt detector is in x direction ($\partial_x T$). Yet there also is a non-negligible thermal gradient in z direction ($\partial_z T$), in the $CrBr_3$ as well as in the Pt detector, allowing for SSE and possible unintended effects occurring in the Pt detector that will be discussed below.

The in-plane magnetic field dependence on the second order nlADMR amplitude $R^{2\omega}_{nl}$ is plotted in Fig. 3(a). We apply a range of fields from 0 T to 7 T for the in-plane rotation measurements at 5 K. At low current (20 μA), we observe a linear increase of $|R^{2\omega}_{nl}|$ from 0 T to 3 T. After 4 T, the magnitude tends to saturate showing only a slight decay [Figs. 3(a) and 3(c)]. At high current (160 μA), we also observe a linear increase of $R^{2\omega}_{nl}$ from 0 T to 4 T, but

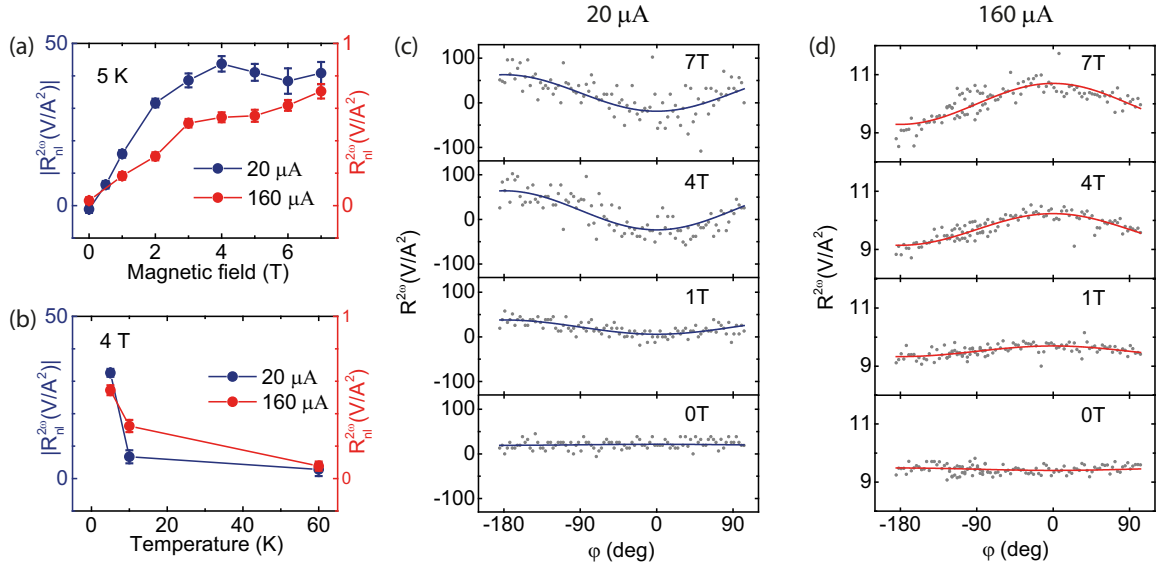

FIG. 3. (a) Magnetic field dependence of $R^{2\omega}_{nl}$ with both low current (20 μA) and high current (160 μA). The fitted cosine amplitude increases with magnetic field until 3 T in both cases. Examples of measured signals are shown in (c) for low bias and in (d) for high bias, with the fitted cosine curves in solid line. (b) The low bias and the high bias signals measured at three different temperatures: 5 K, 10 K, and 60 K. The thermal spin signal measured at 10 K is smaller than 5 K for both low bias and high bias cases.

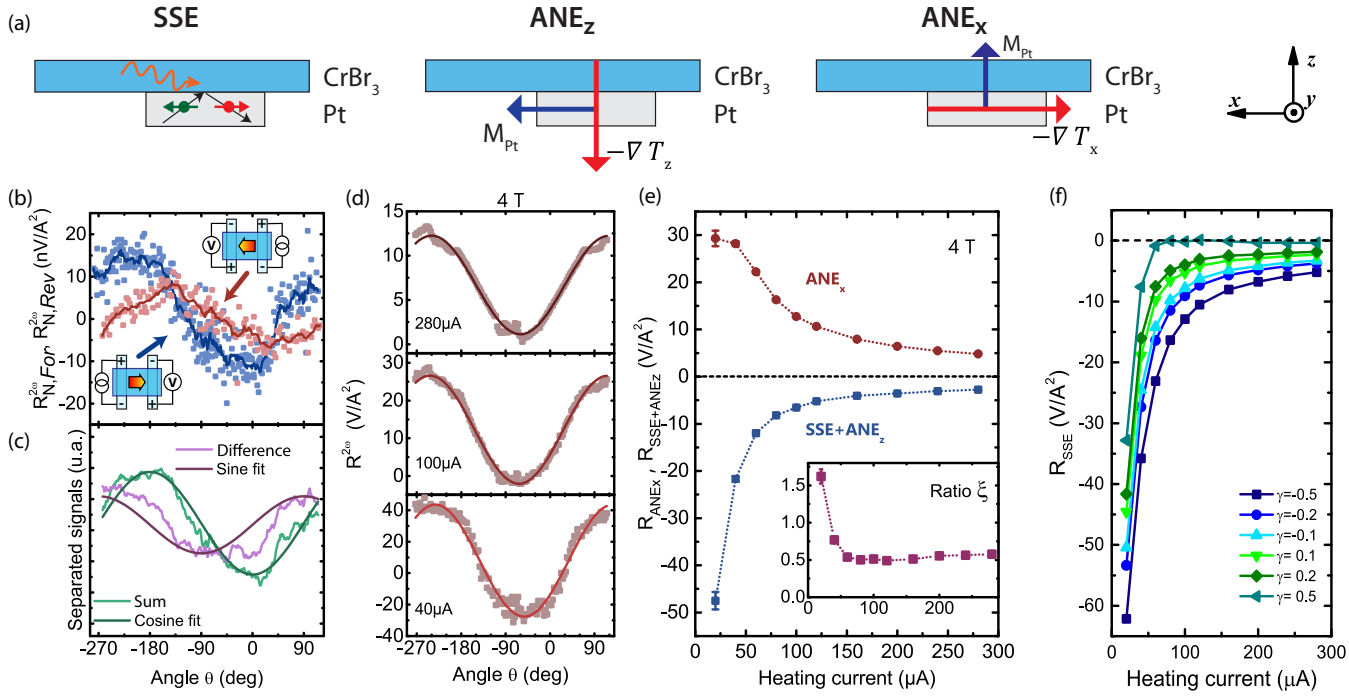

FIG. 4. (a) Schematics of the main effects contributing to the detected signal in OOP-nlADMR, $\varphi = 0°, \theta \in [-180°, 180°]$. (b) Second harmonic nlADMR for the forward (blue) and the reverse (red) configurations measured with applied current of 20 μA. (c) Sum $(R^{2\omega}_{\mathrm{NL,For}} + R^{2\omega}_{\mathrm{NL,Rev}})/2$ (green) and difference $(R^{2\omega}_{\mathrm{NL,For}} - R^{2\omega}_{\mathrm{NL,Rev}})/2$ (purple) of the traces in (b), highlighting contributions that are fitted with $\cos(\theta)$ and $\sin(\theta)$ functions, respectively. (d) Second harmonic nlADMR shown for 40, 100, and 280 μA for an external magnetic field of 4 T rotating in the x-z plane. (e) The current dependence of pANE$_x$ (red) and SSE + pANE$_z$ signals (blue) for the forward configuration. In insets of (e) are given the ratio $\xi = -(R_{\mathrm{SSE}} + R_{\mathrm{pANEz}})/R_{\mathrm{pANEx}}$ (bottom inset). (f) Current dependence of the calculated SSE resistance for a range of $\gamma = \partial_z \mathrm{T}/\partial_x \mathrm{T}$.

with magnitudes about 50 times smaller than $|R^{2\omega}_{\mathrm{nl}}|$ for low current. After 4 T, the magnitude still increases but at a lower rate [Figs. 3(a) and 3(d)]. The lower magnitude at high current is consistent with the reduction of the magnetization expected for a temperature increase due to Joule heating. The origin of the magnetic field dependence remains unclear. As the saturation of the magnetization of trilayer $CrBr_3$ in its hard plane is reported to occur at 400 mT [2], the linear increases cannot be simply explained by the saturation of the magnetization as from an isolated $CrBr_3$ layer and reveals the contribution of additional field dependent effects.

The second order nlADMR is also measured at three different temperatures, 5 K, 10 K, and 60 K, and the fitted amplitudes of $R^{2\omega}_{\mathrm{nl}}$ are shown in Fig. 3(b) for low (20 μA) and high current (160 μA) measured under 4 T. Compared with the signal at 5 K, the fitted cosine amplitude at 10 K decreases for both low and high bias. Far above T_c at 60 K, a very small but nonzero value of $R^{2\omega}_{\mathrm{nl}}$ is observed in our measurements (0.08 ± 0.03 V/A^2 at 160 μA and -3 ± 2 V/A^2 at 20 μA). We attribute this small nonzero value to an artifact from the measurement setup (see Supplemental Material [33]).

We present hereafter a series of out-of-plane nlADMR (OOP-nlADMR) measurements, i.e., fixing $\varphi = 0°$ and varying θ by rotating the magnetic field in the x-z plane, as defined on Fig. 1. Some examples and the current dependence of this OOP-nlADMR are summarized in Fig. 4. The first observation, with Figs. 4(b) and 4(d) as examples, is that all OOP-nlADMR signals exhibit a nonzero angular phase shift varying with the heating current. We investigated the origin of this phase considering the various effects that could add to the SSE signal. Nernst, Seebeck, and spin Nernst magnetoresistance (SNMR) [25,34] effects are discarded as major contributions, either due to the probing geometry or their angular dependence; a detailed description is given in the Supplemental Material [33]. However, the anomalous Nernst effect (ANE), which has already been reported as a possible effect, arising from a proximity induced ferromagnetism into the Pt [24,32,35–38], cannot be ruled out.

Considering a proximity ANE (pANE) in Pt, a transverse pANE voltage ΔV_{pANE} reads

$$\frac{\Delta V_{\mathrm{pANE}}}{L_{\mathrm{Pt}}} = |\nabla V|_y = |-S_{\mathrm{pANE}}(\mathbf{m} \times [-\nabla T])|_y, \qquad (2)$$

where S_{pANE} is the pANE coefficient, $\mathbf{m}$ is the unit vector of direction of the magnetization, and L_{Pt} is the y-axis length of the contact area of Pt with $CrBr_3$. As the magnetization of $CrBr_3$ is expected to saturate for fields beyond 1 T in the hard plane [2,21], we also assume the proximity induced magnetization parallel to the magnetic field at 4 T. Then, two contributions of the pANE are distinguished [Fig. 4(a)]: the pANE signal caused by the IP gradient $\partial_x T$, pANE$_x$, which varies as $\sin(\theta)$, and the pANE signal caused by the OOP gradient $\partial_z T$, pANE$_z$, which varies as $\cos(\theta)$.

The pANE induced by the temperature gradient along x (pANE$_x$) can be isolated from the other signals by changing the heat flow direction. By interchanging the heater and

detector contacts, the heat flow direction along the x axis ($\propto \partial_x T$) is reversed, but the heat flow direction along the z axis ($\propto \partial_z T$) remains the same. Hence the pANE_z contribution will stay unchanged, while the pANE_x will reverse its sign. In Fig. 4(b), we provide a normalized second order nlADMR $R_N^{2\omega} = R^{2\omega} A_{\text{Pt}}/L_{\text{Pt}}$, with A_{Pt} the Pt electrode cross section, at 20 μA and 4 T, for the configuration forward defined in Fig. 1, and the nlADMR from a reversed geometry where heater and detector are interchanged. As the width and length of the two electrodes are different, as well as their interface with $CrBr_3$ possibly, the heating power injected will differ by a small factor. Therefore, our comparison remains only qualitative. Nevertheless, the amplitudes and offsets are alike and the two traces differ mainly by the apparent opposite phase shift.

If both pANE_x and pANE_z contributions are significant in our system, the difference between the forward geometry [Fig. 4(b)] signal and the reverse geometry [Fig. 4(b)] signal will reveal the $\sin(\theta)$ behavior, and the sum of these two signals will reveal the $\cos(\theta)$ behavior. As a result, we obtain the respective traces shown in Fig. 4(c). The good agreement of the fittings on both curves is a confirmation that the pANE is present in the Pt detector.

Based on this observation, we extracted the two contributions for every ADMR at different current and at a constant magnetic field of 4 T, by fitting the expression $R^{2\omega} = R_0^{2\omega} + R_{\text{SSE+pANE}z}\cos\theta + R_{\text{pANE}x}\sin\theta$. The measurements at 40, 100, and 280 μA are shown in Fig. 4(c), and the fitted sinusoidal curve presents the phase shift in each case. The current dependence of the extracted amplitudes is provided in Fig. 4(d). The $R_{\text{SSE+pANE}z}$ and $R_{\text{pANE}x}$ contributions both follow a similar decreasing trend with applied current. While $R_{\text{SSE+pANE}z}$ dominates at 20 and 40 μA, $R_{\text{pANE}x}$ becomes close to twice $R_{\text{SSE+pANE}z}$ at higher current. The variation of the amplitude of $R_{\text{SSE+pANE}z}$ at low currents follows the variation of the signal for IP field rotation in Fig. 2(b); however, the sign reversal for the derived $R_{\text{SSE+pANE}z}$ does not occur in the OOP configuration.

To elucidate the contribution of the spin Seebeck, we introduce the ratio $\xi = -R_{\text{SSE+pANE}z}/R_{\text{pANE}x} = -(R_{\text{SSE}} + R_{\text{pANE}z})/R_{\text{pANE}x}$ of the two contributions [inset of Fig. 4(e)], the ratio $\delta = S^z_{\text{pANE}}/S^x_{\text{pANE}}$ to account for any difference between the IP (S^x_{pANE}) and OOP (S^z_{pANE}) proximity anomalous Nernst coefficients, as well as the ratio $\gamma = \partial_z T/\partial_x T$ of the temperature gradients in Pt. As a result, the SSE contribution to the measured signal simply reads (demonstration in the Supplemental Material [33])

$$R_{\text{SSE}} = R_{\text{pANE}x}(\delta\gamma - \xi). \tag{3}$$

Based upon the fact that the saturated magnetization of $CrBr_3$ has been reported to be of the same magnitude when oriented IP or OOP, we assume $\delta \approx 1$, i.e., $S^z_{\text{pANE}} \approx S^x_{\text{pANE}}$. Following this assumption, the estimated ratio of the two contributions γ lays between -0.20 and 0.15, according to our FEM simulation based on thermal conduction properties of $CrBr_3$ and hBN layers (i.e., the ratio $\eta_{\text{K}} = \kappa_{\text{CrBr}_3}/\kappa_{\text{hBN}}$) (see details in the Supplemental Material [33]). Even using $\delta\gamma = \pm 0.5$ accounting for the possible underestimation of $\partial_z T$ due to the omission of a small heat leakage via the Pt/Au contacts leads on SiO_2, we extract a significant SSE contribution to the nlADMR signal at low heating current, as plotted in Fig. 4(f). We provide the magnetic field dependence of the OOP-nlADMR in Fig. 5. Figure 5(a) shows examples of the evolution of the OOP-nlADMR for 1, 4, and 7 T, for a current fixed to 20 μA. The same operation to separate $\text{pANE}_z + \text{SSE}$ from pANE_x is applied to this measurement set and the amplitude variation of each component is shown in Fig. 5(b) for magnetic fields from 0 to 7 T. The $\text{pANE}_z + \text{SSE}$ variation is comparable to the one measured in in-plane rotation configuration [Fig. 3(a), blue curve], except that we do not observe the high field saturation decrease. The dependence of the pANE_x trace follows a similar increase until 2 T, but shows a slight decrease for 3 and 4 T and increases again to reach the same value as $\text{pANE}_z + \text{SSE}$ at 7 T. This behavior is captured into the ξ ratio that shows a peak above 1.5 for 3 and 4 T and a value remaining around 1 for other field strengths. As the temperature profile is fixed, the difference between $\text{SSE} + \text{pANE}_z$ and pANE_x must be strongly linked to the magnetic properties of the $CrBr_3$/Pt structure.

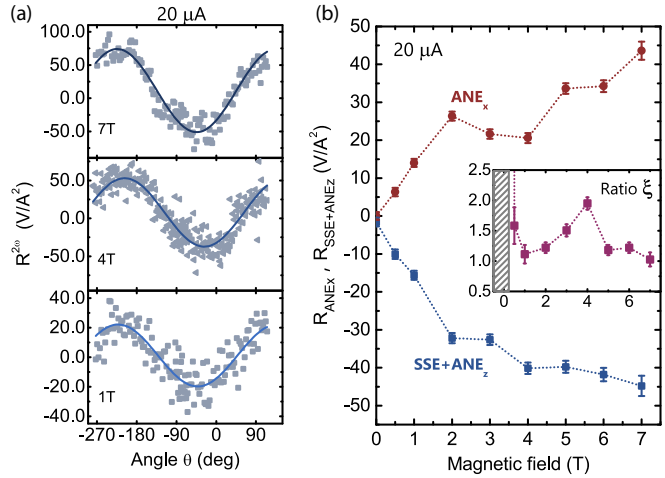

FIG. 5. (a) SSE angular dependence shown for 1, 4, and 7 T, with current fixed to 20 μA at 5 K. (b) Magnetic field dependence of pANE_x and $\text{SSE} + \text{pANE}_z$ signal amplitude for the forward configuration. In the inset of (b) the ratio $\xi = -(R_{\text{SSE}} + R_{\text{pANE}z})/R_{\text{pANE}x}$ is given. See the Supplemental Material [33] for the data extraction in detail.

III. DISCUSSION

By analyzing the OOP-nlADMR, we show that pANE_x presents a different angular dependence than SSE and pANE_z allowing one to separate the two contributions. Despite the lack of insight on the mechanism inducing the magnetization in Pt, this assumption is based on the fact that the magnetic moments emerging on the Pt atoms are imprinted by the moments of $CrBr_3$. Yet the saturated magnetization of $CrBr_3$ has been measured to differ by less than 20% between the orientation along the easy axis and the orientation in the hard plane. Therefore, the induced magnetization in Pt is expected to behave accordingly, leading to a comparable anomalous Nernst coefficient depending on the magnetization value but weakly on its orientation.

A pANE contribution to the ADMR has been identified in Pt/YIG systems as well, but the pANE_z represents at most

5% of the voltage signal, the left 95% being attributed to SSE induced ISHE [32]. Because of the significant magnetic exchange field already noticed in $CrBr_3$ [3,39] as well as the strong temperature gradients involved (beyond two orders of magnitude higher than in [32]), in our $CrBr_3$/Pt system, the pANE cannot be neglected and the SSE signal is at best comparable with the $pANE_z$.

In the Pt/YIG system, the magnon SSE signal decreases with the magnetic field [40]. In Fig. 3(a), we notice that, after 3 T, the fitted amplitude of the low current curve does not change with magnetic field, but $R_{nl}^{2\omega}$ of the high current curve increases linearly with magnetic field. In other words, $R_{nl}^{2\omega}$ at low current tends to decrease where SSE contributes most, compared to the amplitude at high current where the SSE contributes less. Hence our measurements, with support of a temperature distribution simulation, suggest that the high amplitude signal observed at low current is dominated by SSE from $CrBr_3$.

According to the expected angular dependence of the SSE and ANE, the SSE + $pANE_z$ signal should appear in both IP-nlADMR and OOP-nlADMR, while $pANE_x$ should be only detected in OOP-nlADMR. Therefore, the same current dependence of SSE + $pANE_z$ in both configurations is expected. According to the FEM simulation, a reversal of $\partial_z T$ occurs at sufficiently high current, simultaneously in $CrBr_3$ and Pt at the detection interface (see the Supplemental Material [33]). This leads to a reversal of the SSE + $pANE_z$, most likely dominated by ANE in the high current range. However, the sign reversal is only observed in the IP measurements [in Fig. 2(b)], not showing in the OOP measurements after the separation [in Fig. 4(e)]. As the IP and OOP measurements were performed with different cool-down processes, the thermal conductivity is possibly changed at the interface. This implies that the sign reversal current is possibly shifted to a much higher value and therefore not observed in the OOP measurements.

Furthermore, we also suggest that a quantitative discrimination between pANE and SSE is possible. We provide an indicative estimation of the magnitude of the SSE based on the assumption that the pANE coefficient is equal for ANE_x and ANE_z. By far, we are limited by the current knowledge on the material properties of the 2D magnet. However, if the thermal conduction profiles and the magnetization dynamics are characterized concretely, a more accurate separation of the two spin-caloritronic effects can be realized.

Nevertheless, the magnetic field dependence of $pANE_x$ and SSE + $pANE_z$ and the difference between them bring new questions. The ANE scales with the magnetization via the coefficient S_{pANE}. The nonmonotonic field dependence of $pANE_x$ suggests a complex evolution of the induced magnetization in Pt, due to either the presence of magnetic domains or any additional interaction at the interface.

IV. CONCLUSIONS

To conclude, we demonstrate the relevance of the full hBN encapsulation and the bottom contacting design to enable the integration of air-reactive materials such as $CrBr_3$, for studying spin-caloritronic effects in 2D magnets. By using second order nlADMR measurement on such an encapsulated $CrBr_3$/Pt device, we reveal, by detecting the presence of a proximity ANE voltage, a significant proximity induced magnetism from $CrBr_3$ into the adjacent Pt contacts. With reasonable assumptions, we conjecture about the presence of a weak SSE, dominating the signal in the low current regime, while the pANE prevails for currents above 60 μA. The nontrivial magnetic field dependence of the separated effects leaves open questions as for the current understanding of magnetic effects at the interface of heavy metal and 2D magnets. The encapsulation shows itself as an elegant technique to address these questions in deeper investigations of air-degradable 2D materials, and opens the way to future magnon transport studies.

V. METHODS

$CrBr_3$ and hBN crystals are provided by a commercial company HQgraphene. $CrBr_3$ is an air sensitive material. To study magnonics with $CrBr_3$ in a nonlocal geometry, we encapsulate a 7-nm-thin chromium tribromide flake and platinum (Pt) strips into two hexagonal boron nitride (hBN) layers (top layer and bottom layer). The stacking of van der Waals materials was performed in a glove box filled with inert gas argon by using standard PC/PDMS dry transfer method. Pt strips were first grown on bottom hBN. After that $CrBr_3$ with a top hBN thin layer was transferred on top of the Pt strips. See the Supplemental Material [33] for more details in fabrication process.

ACKNOWLEDGMENTS

The authors thank Prof. J. Ye and P. Wan for granting us access to their transfer system in an Ar glove box. We thank J. G. Holstein, H. de Vries, H. Adema, and T. J. Schouten for technical assistance. We acknowledge fruitful discussions with G. R. Hoogeboom, A. A. Kaverzin, and J. Liu. This project has received funding from the Dutch Foundation for Fundamental Research on Matter (FOM, now known as NWO-I) as a part of the Netherlands Organization for Scientific Research (NWO), the European Union's Horizon 2020 research and innovation programme under Grants Agreement No. 696656 and No. 785219 (Graphene Flagship Core 1 and Core 2), and Zernike Institute for Advanced Materials. M.H.D.G. acknowledges support from NWO VENI 15093.

[1] B. Huang, G. Clark, E. Navarro-moratalla, D. R. Klein, R. Cheng, K. L. Seyler, D. Zhong, E. Schmidgall, M. A. Mcguire, D. H. Cobden, W. Yao, D. Xiao, P. Jarillo-herrero, and X. Xu, Waals crystal down to the monolayer limit, Nature (London) **546**, 270 (2017).

[2] H. H. Kim, B. Yang, S. Li, S. Jiang, C. Jin, Z. Tao, G. Nichols, F. Sfigakis, S. Zhong, C. Li, S. Tian, D. G. Cory, G. X. Miao, J. Shan, K. F. Mak, H. Lei, K. Sun, L. Zhao, and A. W. Tsen, Evolution of interlayer and intralayer magnetism in three atomically thin

chromium trihalides, Proc. Natl. Acad. Sci. U.S.A. **166**, 11131 (2019).

[3] M. Kim, P. Kumaravadivel, J. Birkbeck, W. Kuang, S. G. Xu, D. G. Hopkinson, J. Knolle, P. A. McClarty, A. I. Berdyugin, M. Ben Shalom, R. V. Gorbachev, S. J. Haigh, S. Liu, J. H. Edgar, K. S. Novoselov, I. V. Grigorieva, and A. K. Geim, Micromagnetometry of two-dimensional ferromagnets, Nat. Electron. **2**, 457 (2019).

[4] F. Bloch, Zur theorie des ferromagnetismus, Z. Phys. **61**, 206 (1930).

[5] C. Kittel, *Introduction to Solid State Physics*, 8th ed. (Wiley, New York, 2004).

[6] J. Shan, *Coupled Charge, Spin and Heat Transport in Metal-insulator Hybrid Systems* (Rijksuniversiteit Groningen, Groningen, 2018).

[7] Y. Tserkovnyak, A. Brataas, and G. E. W. Bauer, Enhanced Gilbert Damping in Thin Ferromagnetic Films, Phys. Rev. Lett. **88**, 117601 (2002).

[8] K. Uchida, J. Xiao, H. Adachi, J. Ohe, S. Takahashi, J. Ieda, T. Ota, Y. Kajiwara, H. Umezawa, H. Kawai, G. E. W. Bauer, S. Maekawa, and E. Saitoh, Spin Seebeck insulator, Nat. Mater. **9**, 894 (2010).

[9] L. Cornelissen, J. Liu, R. Duine, J. B. Youssef, and B. Van Wees, Long-distance transport of magnon spin information in a magnetic insulator at room temperature, Nat. Phys. **11**, 1022 (2015).

[10] R. Lebrun, A. Ross, S. Bender, A. Qaiumzadeh, L. Baldrati, J. Cramer, A. Brataas, R. Duine, and M. Kläui, Tunable long-distance spin transport in a crystalline antiferromagnetic iron oxide, Nature (London) **561**, 222 (2018).

[11] C. Hahn, G. De Loubens, V. V. Naletov, J. B. Youssef, O. Klein, and M. Viret, Conduction of spin currents through insulating antiferromagnetic oxides, EPL (Europhys. Lett.) **108**, 57005 (2014).

[12] H. Wu, L. Huang, C. Fang, B. S. Yang, C. H. Wan, G. Q. Yu, J. F. Feng, H. X. Wei, and X. F. Han, Magnon Valve Effect between Two Magnetic Insulators, Phys. Rev. Lett. **120**, 097205 (2018).

[13] A. V. Chumak, A. A. Serga, and B. Hillebrands, Magnon transistor for all-magnon data processing, Nat. Commun. **5**, 4700 (2014).

[14] S. S. Pershoguba, S. Banerjee, J. C. Lashley, J. Park, H. Ågren, G. Aeppli, and A. V. Balatsky, Dirac Magnons in Honeycomb Ferromagnets, Phys. Rev. X **8**, 011010 (2018).

[15] R. Cheng, S. Okamoto, and D. Xiao, Spin Nernst Effect of Magnons in Collinear Antiferromagnets, Phys. Rev. Lett. **117**, 217202 (2016).

[16] K. Nakata, S. K. Kim, J. Klinovaja, and D. Loss, Magnonic topological insulators in antiferromagnets, Phys. Rev. B **96**, 224414 (2017).

[17] J. Xu, W. A. Phelan, and C. L. Chien, Large anomalous Nernst effect in a van der Waals ferromagnet Fe_3GeTe_2, Nano Lett. **19**, 8250 (2019).

[18] D. Ghazaryan, M. T. Greenaway, Z. Wang, V. H. Guarochico-Moreira, I. J. Vera-Marun, J. Yin, Y. Liao, S. V. Morozov, O. Kristanovski, A. I. Lichtenstein, M. I. Katsnelson, F. Withers, A. Mishchenko, L. Eaves, A. K. Geim, K. S. Novoselov, and A. Misra, Magnon-assisted tunneling in van der Waals heterostructures based on $CrBr_3$, Nat. Electron. **1**, 344 (2018).

[19] W. Xing, L. Qiu, X. Wang, Y. Yao, Y. Ma, R. Cai, S. Jia, X. C. Xie, and W. Han, Magnon Transport in Quasi-two-dimensional van der Waals Antiferromagnets, Phys. Rev. X **9**, 011026 (2019).

[20] I. Tsubokawa, On the magnetic properties of a $CrBr_3$ single crystal, J. Phys. Soc. Jpn. **15**, 1664 (1960).

[21] N. Richter, D. Weber, F. Martin, N. Singh, U. Schwingenschlögl, B. V. Lotsch, and M. Kläui, Temperature-dependent magnetic anisotropy in the layered magnetic semiconductors CrI_3 and $CrBr_3$, Phys. Rev. Materials **2**, 024004 (2018).

[22] H. Nakayama, M. Althammer, Y.-T. Chen, K. Uchida, Y. Kajiwara, D. Kikuchi, T. Ohtani, S. Geprägs, M. Opel, S. Takahashi *et al.*, Spin Hall Magnetoresistance Induced by a Nonequilibrium Proximity Effect, Phys. Rev. Lett. **110**, 206601 (2013).

[23] T. Kikkawa, K. Uchida, S. Daimon, Y. Shiomi, H. Adachi, Z. Qiu, D. Hou, X.-F. Jin, S. Maekawa, and E. Saitoh, Separation of longitudinal spin Seebeck effect from anomalous Nernst effect: Determination of origin of transverse thermoelectric voltage in metal/insulator junctions, Phys. Rev. B **88**, 214403 (2013).

[24] D. Meier, D. Reinhardt, M. van Straaten, C. Klewe, M. Althammer, M. Schreier, S. T. B. Goennenwein, A. Gupta, M. Schmid, C. H. Back, J.-M. Schmalhorst, T. Kuschel, and G. Reiss, Longitudinal spin Seebeck effect contribution in transverse spin Seebeck effect experiments in Pt/YIG and Pt/NFO, Nat. Commun. **6**, 8211 (2015).

[25] S. Meyer, Y.-T. Chen, S. Wimmer, M. Althammer, T. Wimmer, R. Schlitz, S. Geprägs, H. Huebl, D. Ködderitzsch, H. Ebert, G. E. W. Bauer, R. Gross, and S. T. B. Goennenwein, Observation of the spin Nernst effect, Nat. Mater. **16**, 977 (2017).

[26] C. O. Avci, E. Rosenberg, M. Huang, J. Bauer, C. A. Ross, and G. S. D. Beach, Nonlocal Detection of Out-of-Plane Magnetization in a Magnetic Insulator by Thermal Spin Drag, Phys. Rev. Lett. **124**, 027701 (2020).

[27] P. Zomer, S. Dash, N. Tombros, and B. Van Wees, A transfer technique for high mobility graphene devices on commercially available hexagonal boron nitride, Appl. Phys. Lett. **99**, 232104 (2011).

[28] M. Schreier, G. E. W. Bauer, V. I. Vasyuchka, J. Flipse, K. ichi Uchida, J. Lotze, V. Lauer, A. V. Chumak, A. A. Serga, S. Daimon, T. Kikkawa, E. Saitoh, B. J. van Wees, B. Hillebrands, R. Gross, and S. T. B. Goennenwein, Sign of inverse spin Hall voltages generated by ferromagnetic resonance and temperature gradients in yttrium iron garnet platinum bilayers, J. Phys. D **48**, 025001 (2014).

[29] L. Cornelissen, Magnon spin transport in magnetic insulators, Ph.D. thesis, University of Groningen, 2018.

[30] F. L. Bakker, A. Slachter, J.-P. Adam, and B. J. van Wees, Interplay of Peltier and Seebeck Effects in Nanoscale Nonlocal Spin Valves, Phys. Rev. Lett. **105**, 136601 (2010).

[31] J. F. Sierra, I. Neumann, J. Cuppens, B. Raes, M. V. Costache, and S. O. Valenzuela, Thermoelectric spin voltage in graphene, Nat. Nanotechnol. **13**, 107 (2018).

[32] T. Kikkawa, K. Uchida, Y. Shiomi, Z. Qiu, D. Hou, D. Tian, H. Nakayama, X.-F. Jin, and E. Saitoh, Longitudinal Spin Seebeck Effect Free from the Proximity Nernst Effect, Phys. Rev. Lett. **110**, 067207 (2013).

[33] See Supplemental Material at http://link.aps.org/supplemental/10.1103/PhysRevB.101.205407 for supplemental data and

simulations to the main article, as well as an overview of spin caloritronic phenomena in the device, including Refs. [41–46] .

[34] D.-J. Kim, C.-Y. Jeon, J.-G. Choi, J. W. Lee, S. Surabhi, J.-R. Jeong, K.-J. Lee, and B.-G. Park, Observation of transverse spin Nernst magnetoresistance induced by thermal spin current in ferromagnet/non-magnet bilayers, Nat. Commun. **8**, 1400 (2017).

[35] J. C. Leutenantsmeyer, A. A. Kaverzin, M. Wojtaszek, and B. J. van Wees, Proximity induced room temperature ferromagnetism in graphene probed with spin currents, 2D Mater. **4**, 014001 (2016).

[36] K. Zollner, M. Gmitra, T. Frank, and J. Fabian, Theory of proximity-induced exchange coupling in graphene on hBN/(Co, Ni), Phys. Rev. B **94**, 155441 (2016).

[37] G. Y. Guo, Q. Niu, and N. Nagaosa, Anomalous Nernst and Hall effects in magnetized platinum and palladium, Phys. Rev. B **89**, 214406 (2014).

[38] Y. M. Lu, Y. Choi, C. M. Ortega, X. M. Cheng, J. W. Cai, S. Y. Huang, L. Sun, and C. L. Chien, Pt Magnetic Polarization on $Y_3Fe_5O_{12}$ and Magnetotransport Characteristics, Phys. Rev. Lett. **110**, 147207 (2013).

[39] C. Tang, Z. Zhang, S. Lai, Q. Tan, and W.-b. Gao, Magnetic proximity effect in graphene/ $CrBr_3$ van der Waals heterostructures, Adv. Mater. **32**, 1908498 (2020).

[40] L. J. Cornelissen, K. J. H. Peters, G. E. W. Bauer, R. A. Duine, and B. J. van Wees, Magnon spin transport driven by the magnon chemical potential in a magnetic insulator, Phys. Rev. B **94**, 014412 (2016).

[41] M. Isasa, E. Villamor, L. E. Hueso, M. Gradhand, and F. Casanova, Temperature dependence of spin diffusion length and spin Hall angle in Au and Pt, Phys. Rev. B **91**, 024402 (2015).

[42] E. K. Sichel, R. E. Miller, M. S. Abrahams, and C. J. Buiocchi, Heat capacity and thermal conductivity of hexagonal pyrolytic boron nitride, Phys. Rev. B **13**, 4607 (1976).

[43] M. M. Sadeghi, M. T. Pettes, and L. Shi, Thermal transport in graphene, Solid State Commun. **152**, 1321 (2012).

[44] N. Cusack and P. Kendall, The absolute scale of thermoelectric power at high temperature, Proc. Phys. Soc. **72**, 898 (1958).

[45] N. Vlietstra, J. Shan, V. Castel, B. J. van Wees, and J. Ben Youssef, Spin-Hall magnetoresistance in platinum on yttrium iron garnet: Dependence on platinum thickness and in-plane/out-of-plane magnetization, Phys. Rev. B **87**, 184421 (2013).

[46] J. D. Renteria, S. Ramirez, H. Malekpour, B. Alonso, A. Centeno, A. Zurutuza, A. I. Cocemasov, D. L. Nika, and A. A. Balandin, Strongly anisotropic thermal conductivity of free-standing reduced graphene oxide films annealed at high temperature, Adv. Funct. Mater. **25**, 4664 (2015).